




Article

General Current Control of Six-Phase-Based Non-Isolated Integrated On-Board Charger with Low Order Harmonic Compensation

Mahmoud S. Abdel-Majeed ¹, Abdullah Shawier ¹, Ayman S. Abdel-Khalik ^{1,*}, Mostafa S. Hamad ², Mohamed M. Sedky ¹ and Noha A. Elmalhy ¹

¹ Department of Electrical Engineering, Alexandria University, Alexandria 21544, Egypt; es-mahmoud.said1415@alexu.edu.eg (M.S.A.-M.); es-abdallh.shawier@alexu.edu.eg (A.S.); Mohamed.sedky@alexu.edu.eg (M.M.S.); noha.elmalhy@alexu.edu.eg (N.A.E.)

² Department of Electrical and Control Engineering, Arab Academy for Science, Technology and Maritime Transport, Alexandria 21913, Egypt; mostafa.hamad@staff.aast.edu

* Correspondence: ayman.abdel-khalik@alexu.edu.eg

Abstract: Electric vehicle charging technology has recently witnessed massive developments due to its significant role in the ever-growing number of electric vehicles on the market. The integrated on-board charger technology (IOBC) represents an effective and attractive solution to reduce EV size, cost, and weight. IOBC technology employs propulsion components, such as the motor and its converter, in the charging process. The main objective of IOBC is to achieve the maximum charging current with zero average/pulsating torque so that mechanical interlocking can be dispensed. Recently, some of the IOBC topologies have adopted machines with six-phase stators to exploit the many advantages of multiphase-based systems. This paper investigates the effect of the winding design, namely, chorded or un-chorded designs, as well as the winding configuration, namely, dual three-phase, asymmetrical, or symmetrical winding configurations, on the current quality of a six-phase-based non-isolated IOBC. The relation between the winding design and the induced low order harmonics in the charging current is first clarified. The required current controller structure is then proposed, which ensures balanced grid line currents with high quality, under either healthy or one-phase fault conditions. Finally, a comparative study between all available designs with the proposed current controller is carried out to validate the theoretical findings.



Citation: Abdel-Majeed, M.S.; Shawier, A.; Abdel-Khalik, A.S.; Hamad, M.S.; Sedky, M.M.; Elmalhy, N.A. General Current Control of Six-Phase-Based Non-Isolated Integrated On-Board Charger with Low Order Harmonic Compensation. *Sustainability* **2022**, *14*, 1088. <https://doi.org/10.3390/su14031088>

Academic Editor: Mohamed Abdelrahem

Received: 18 December 2021

Accepted: 15 January 2022

Published: 18 January 2022

Publisher's Note: MDPI stays neutral with regard to jurisdictional claims in published maps and institutional affiliations.



Copyright: © 2022 by the authors. Licensee MDPI, Basel, Switzerland. This article is an open access article distributed under the terms and conditions of the Creative Commons Attribution (CC BY) license (<https://creativecommons.org/licenses/by/4.0/>).

Keywords: six phase; dual three-phase; asymmetrical six-phase; symmetrical six-phase; low order space harmonics; magneto-motive force; harmonic compensation; PR controller; battery charging; integrated onboard battery chargers

1. Introduction

A clean, energy-based transportation is now globally required as a major step to hold back climate change and the greenhouse effect. Electric vehicles (EVs) impose themselves as a promising alternative to the conventional diesel engine vehicles. Nowadays, extensive investments are focusing on developing EV-based technologies and their components, such as electric motor design, converter design, innovative control techniques, batteries, and battery chargers [1]. However, one of the major challenges that has curbed the use of EVs widely is the limited range that car can go on one charge [2]. This, in turn, sheds light on developing different charging technologies of EVs, starting from battery design and ending up with charger types. In this context, EV chargers are classified into two main categories: off-board and on-board chargers [3].

Albeit off-board chargers are distinguished by their safety and fast charging competence, this option entails dedicated resources and infrastructure [4]. On the other hand, on-board chargers offer a simple charging solution thanks to their capability of charging

directly from AC plugs. However, the charging time is relatively slow due to onboard weight, volume, and cost constraints.

Lately, the idea of integrated on-board chargers has emerged as an alternative solution to overcome the limitations of on-board chargers [5]. IOBCs employ propulsion components, namely, the converter and motor, in the charging process. Thus, the power flows from grid to the battery through the converter, while the motor acts as a smoothing filter. Examples of some single-phase IOBCs are reviewed in [4]. Due to the limited power range of single-phase-based IOBCs, the three-phase IOBCs have shown accelerating potentials in recent literature [6,7]. The main control challenge of this technology is to ensure zero torque production under charging. From the machine point of view, based on the comprehensive review of EVs given in [8], the permanent magnet and induction machines are likely the most common types employed in EVs [9].

Recently, multiphase machines are being favored for EV drivelines over their three-phase counterparts. The fault-tolerance and reduced converter per-phase current/voltage ratings are the main merits of multiphase machines [10,11]. Different multiphase-based IOBC topologies have been proposed in the available literature [10,12,13]. Currently, the six-phase induction machine (SPIM) has been preferred in recent literature to be a reasonable/compromised alternative for three-phase motors. Moreover, SPIM offers less complexity, is cost-effective, and is a more reliable solution compared to other phase orders. The SPIM can easily be rewound using the same standard three-phase stator frames with, theoretically, no practical constraints, besides its capability of being driven using off-the-shelf three-phase converters [14,15]. In the literature, six-phase machines have been proposed with three different winding layouts, namely, dual three-phase (D3P), asymmetrical six-phase (A6P), and symmetrical six-phase (S6P) [16]. Another novel winding layout for six-phase machines, known as pseudo six-phase, has proved to offer a 5% enhancement in the torque density over conventional six-phase winding [17].

Most of the up-to-date literature has emphasized controlling the SPIM under propulsion mode. However, considering SPIM in an IOBC system raises more challenges when standard current controllers are to be preserved. The control technique of a SPIM-based IOBC system should control the machine phase currents in a manner that ensures zero torque production during charging mode. To this end, literature has suggested different solutions to ensure zero torque production. For instance, the concept of phase transformation represents one of the proposed solutions that has been applied to symmetrical and asymmetrical SPIM-based IOBCs to nullify the torque production during battery pack charging [13,18]. In this latter technique, the machine stator is connected to the grid using a two-secondary winding transformer, while the converter is controlled in such a way as to ensure zero fundamental ($\alpha\beta$) current components using conventional PI controllers. In [18], an alternative topology has been proposed and applied to either A6P or S6P machines, which enables fast-charging up to 100% of the traction power rating. The so-called vector PI resonant controller has been employed to control the system under either propulsion or charging modes. Another non-isolated IOBC topology that achieves 100% charging/propulsion power ratio has been proposed in [19]. Even though this latter topology can successfully cancel out the average torque production, a notable pulsating torque component still exists. An attempt to reduce the converter complexity was suggested in [20] by employing a nine-switch converter to drive a symmetrical SPIM in both charging and traction with a simple hardware reconfiguration.

Although most of the conducted research related to multiphase-based IOBC has been done under healthy conditions, [10] has taken the initiative to control a nine-phase machine-based IOBC under postfault cases. The same objective has also been introduced in [21] for a SPIM-based IOBC under postfault operation. However, this technique has only been able to cancel out the average torque production with a significant torque component due to the generated pulsating fundamental flux component.

Some recent studies have compared the symmetrical and asymmetrical winding configurations under both healthy as well as fault conditions [22,23]. A thorough comparative

study between the three variations of six-phase winding configurations by investigating their air gap flux distributions under different excitations is provided by [24]. The study showed that the D3P and S6P connections are very similar, whereas the equivalent reactance of an A6P connected winding is slightly higher due to the effect of leakage mutual inductance of a double layer winding design [24]. The effect of stator winding connection on the harmonic mapping was also investigated by plotting the MMF distributions and their harmonic spectra under different excitations [24].

To the best of the authors' knowledge, literature has not investigated the effect of stator winding design as well as winding configuration of a SPIM-based non-isolated IOBC system on the induced low order harmonic currents and the line current quality under charging mode. All available literature has regarded the machine as a pure series inductance, while it has completely ignored the possible induced back emf harmonic voltage components due to phase-belt low order space harmonics. To this end, this paper investigates a SPIM-based IOBC with the three available winding configurations, namely, D3P, ASP, and S6P, under both healthy case (HC) and single open phase fault (1OPF) case. The effect of winding chording on the induced low order MMF space harmonics is first investigated to clarify the possible sources of these harmonic current components under charging. Hence, a general current controller structure with harmonic compensation (HC) for a general six-phase-based winding topology is then proposed for both healthy and postfault operation.

The paper is organized as follows. Section 2 discusses the proposed winding connection with the grid. Section 3 depicts the MMF harmonic spectra due to different sequence current excitations related to each winding layout. The required optimum set of phase currents under both healthy and 1OPF case are derived in Section 4 for the three possible connections. The proposed controller structure that ensures the main objectives while respecting the imposed constraints under charging is then introduced in Section 5. The experimental validation is discussed in Section 6. Finally, the paper is summarized in Section 7.

2. Six-Phase-Based IOBC Connection with Grid

This section discusses the required connection of the stator winding to integrate a general SPIM-based non-isolated IOBC with the grid. When non-isolated IOBC topologies are employed, the machine acts as a single neutral (1N) SPIM; therefore, the nonavoidable circulating $i_{0+,0-}$ current component should be properly controlled to ensure high-quality phase currents. The IOBC connection will be evaluated for the three winding layouts (D3P, A6P, and S6P) with and without winding chording employed.

For the three winding configurations of a SPIM, namely, D3P, A6P and S6P, the corresponding arbitrary spatial phase-shift angle δ between the two three-phase winding sets are 0° , 30° , and 60° , respectively. The six-phase machine has three main subspaces, namely, the fundamental subspace ($\alpha\beta$), secondary subspace (xy), and zero subspace (0^+0^-). The vector space decomposition (VSD) [24] matrix that correlates the sequence components (i.e., $\alpha\beta$, xy , and 0^+0^-) and the phase quantity components (current or voltage) with a general arbitrary angle, δ , is given by (1).

$$T_{VSD} = \frac{1}{3} \times \begin{bmatrix} 1 & \cos\left(\frac{2\pi}{3}\right) & \cos\left(\frac{4\pi}{3}\right) & \cos\delta & \cos\left(\delta + \frac{2\pi}{3}\right) & \cos\left(\delta + \frac{4\pi}{3}\right) \\ 0 & \sin\left(\frac{2\pi}{3}\right) & \sin\left(\frac{4\pi}{3}\right) & \cos\delta & \sin\left(\delta + \frac{2\pi}{3}\right) & \sin\left(\delta + \frac{4\pi}{3}\right) \\ 1 & \cos\left(\frac{4\pi}{3}\right) & \cos\left(\frac{2\pi}{3}\right) & \cos\delta & -\cos\left(\delta + \frac{2\pi}{3}\right) & -\cos\left(\delta + \frac{4\pi}{3}\right) \\ 0 & \sin\left(\frac{4\pi}{3}\right) & \sin\left(\frac{2\pi}{3}\right) & \cos\delta & -\sin\left(\delta + \frac{2\pi}{3}\right) & -\sin\left(\delta + \frac{4\pi}{3}\right) \\ 1 & \frac{1}{1} & 1 & \frac{0}{1} & 0 & 0 \\ 0 & 0 & 0 & 1 & 1 & 1 \end{bmatrix} \quad (1)$$

$$\begin{bmatrix} i_s^{\alpha\beta} \\ i_s^{xy} \\ i_s^{0+0-} \end{bmatrix}_{6 \times 1} = T_{VSD} \begin{bmatrix} i_s^{a_1 \rightarrow c_1} \\ i_s^{a_2 \rightarrow c_2} \end{bmatrix}_{6 \times 1} \quad (2)$$

Under propulsion mode, the fundamental subspace current components, $i_s^{\alpha\beta}$, are exclusively utilized for torque production, while other sequence currents are controlled to zero to ensure a ripple-free torque production with high quality phase currents. On the other hand, the charging mode utilizes the secondary subspace current components, i_s^{xy} , only, while other sequence currents are controlled to zero. Under propulsion mode, and by setting the $i_s^{\alpha\beta}$ current components to $I\angle 0$ and $I\angle -90$, the resultant phase currents from the inverse of (2) will yield a phase shift angle between the three-phase sets of 0° , 30° , and for the D3P, A6P, and S6P machines, respectively, as clarified in Figure 1. Meanwhile, under charging mode, setting the i_s^{xy} current components to $I\angle 0$ and $I\angle 90$ results in set of phase currents with a phase shift angle between the two three-phase sets of 180° , 210° , and 240° for the D3P, A6P, and S6P machines, respectively, as shown in Figure 1.

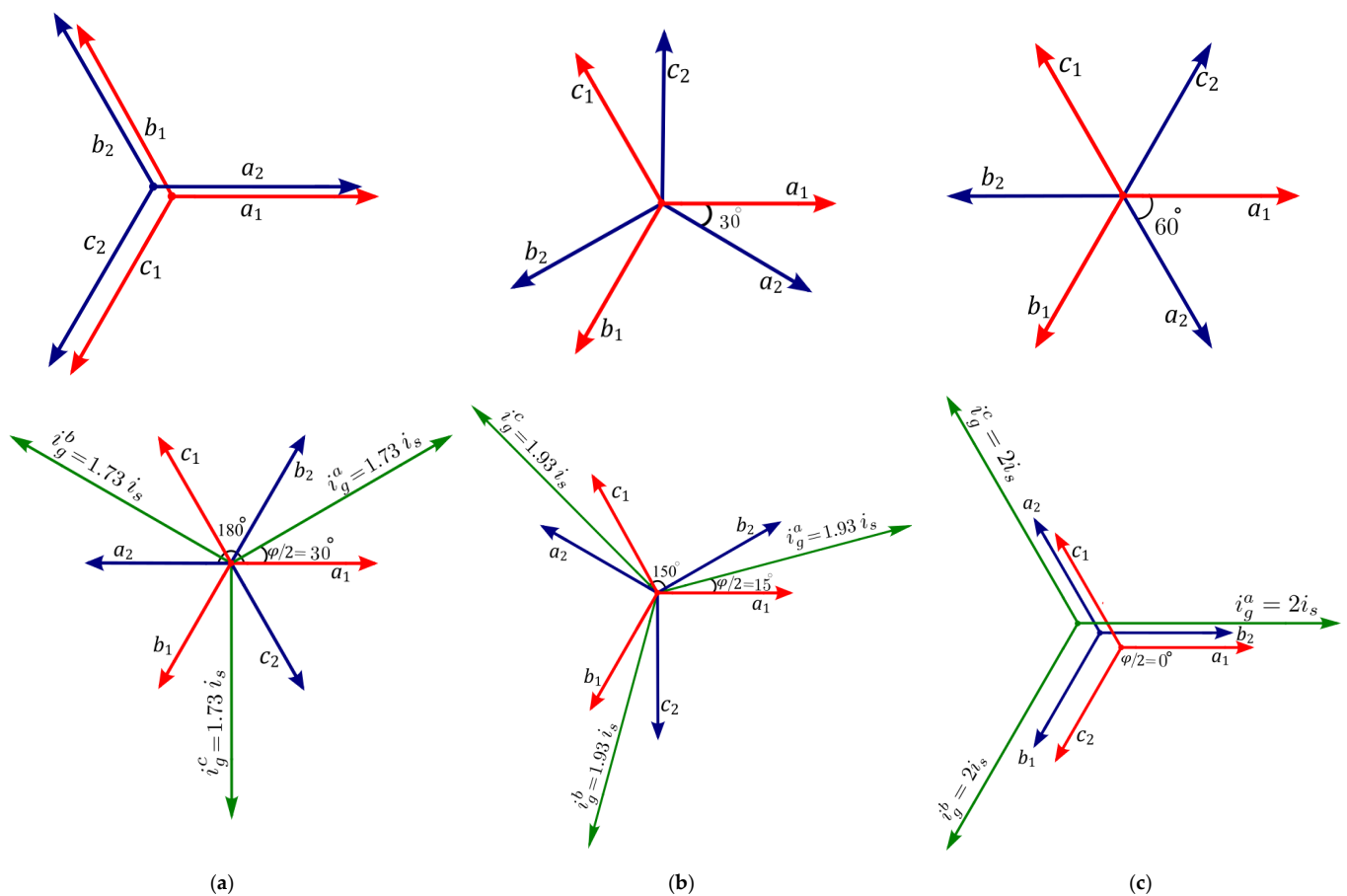


Figure 1. Phase and line currents of SPIM for all three types of SPIM (a) D3P, (b) A6P, and (c) S6P, under propulsion mode (upper plots) and charging mode (lower plots).

Based on the current phasors under charging given in Figure 1, the suggested external connection of the three available configurations to integrate the six-phase machine with the grid are shown in Figure 2. This connection maximizes the charging line current while nullifying the torque production inside the machine. By looking at the current phasor diagram under xy excitation shown in Figure 1, adding $(i_s^{a_1}$ and $i_s^{b_2})$, $(i_s^{b_1}$ and $i_s^{c_2})$, and $(i_s^{c_1}$ and $i_s^{a_2})$ together result in a line current magnitude equal to $2 \cos 30^\circ$, $2 \cos 15^\circ$, and $2 \cos 0^\circ$ times the phase current for the three connections, respectively. Therefore, connecting the end terminals $(a_1$ and $b_2)$, $(b_1$ and $c_2)$, and $(c_1$ and $a_2)$ of the six-phase stator together with the

grid lines (a_g , b_g , and c_g), while exciting the xy subspace only, will maximize the charging line currents and ensure zero torque production.

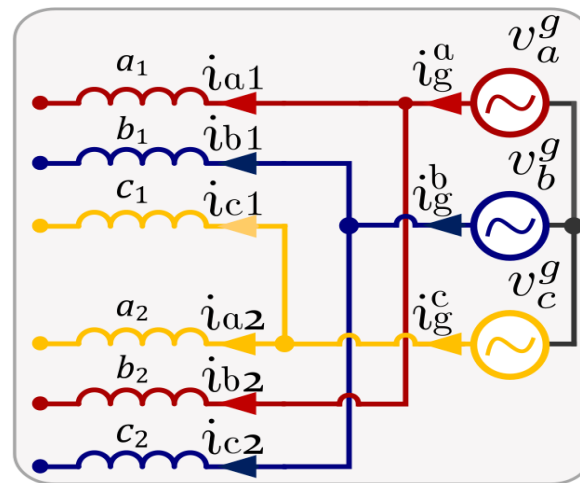


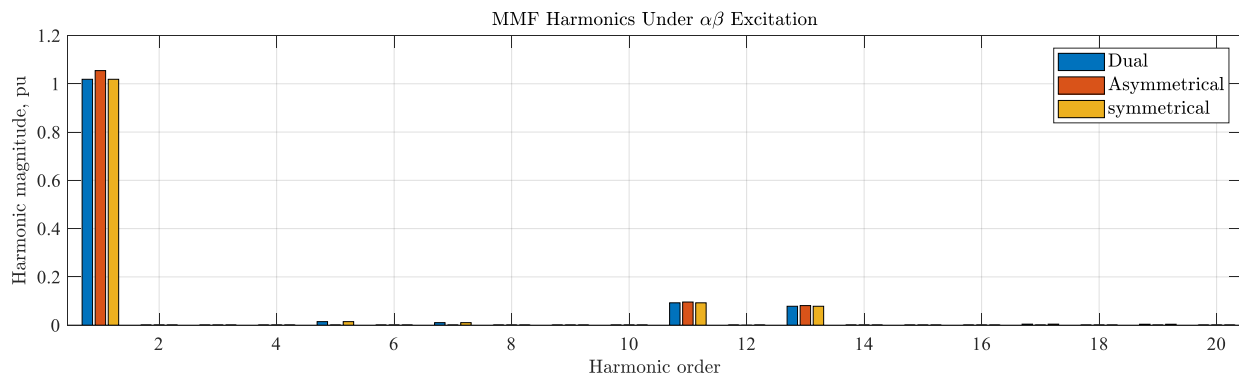
Figure 2. Proposed connection for SPIM based IOBC.

3. MMF Spectra of Different Winding Layouts

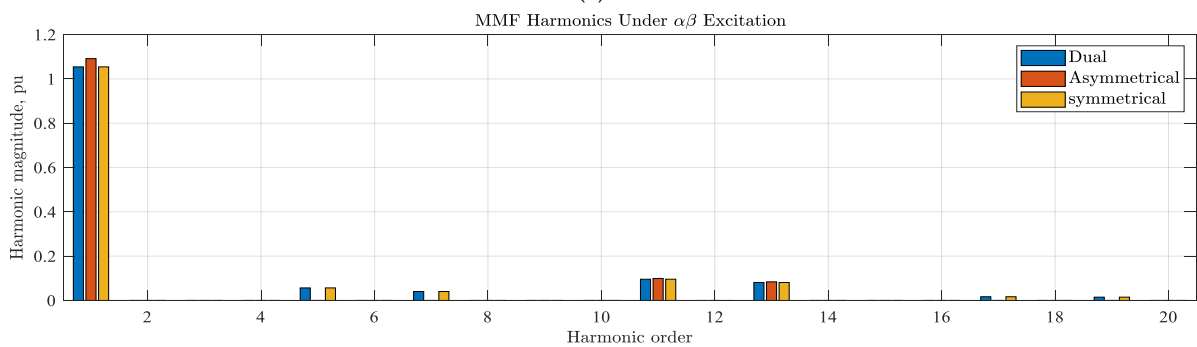
In AC winding, coil chording is usually employed to obtain a high-quality flux distribution under fundamental $\alpha\beta$ excitation. In all available literature, the flux distributions under non-fundamental subspace excitations (i.e., xy and 0^+ , 0^-) were ideally assumed to be zero. This assumption was recently found to be rather ideal, especially when winding chording is applied to improve the fundamental flux [24]. In this section, the effect of winding chording on the stator MMF spectra is investigated and compared with fully pitched stators for the three available configurations. Since the IOBC control algorithm utilizes only the xy subspace in the charging process, the focus will be directed to the MMF spectra under xy excitation. A 24-slot, 4-pole stator is employed for this comparison. It has been shown in [24] that a 24-slot with 12 phases can be used to construct any of the 3 6-phase winding layouts by externally connecting certain pairs of phases in such a way as to produce 6 terminals only. In the available literature, a 5/6 coil pitch is commonly employed in practical six-phase induction machines [24], which will also be used for the chorded winding case in this study.

Figure 3 shows the MMF spectra under $\alpha\beta$ excitation (propulsion mode). It is clear that chording the stator winding with one slot is essential under D3P and S6P to minimize the 5th and 7th low order space harmonics; however, it affects the fundamental component, when compared with the A6P case.

On the other hand, Figure 4 illustrates the MMF spectra under xy excitation (charging mode). It is obvious that both D3P and S6P have the same MMF spectra under chorded winding with clear, even harmonic components, indicating asymmetrical flux distribution under this excitation profile. Although these space harmonics will increase the leakage inductance of the xy subspace [24], which will improve current quality under charging, they are also expected to induce undesirable harmonics in the phase currents. On the other hand, the two winding layouts (D3P and S6P) correspond to zero magnetizing flux when fully pitch winding is employed. Figure 4 also shows the MMF spectra of an A6P stator, where the 5th and 7th harmonics represent the dominate harmonics in both chorded and un-chorded windings. Clearly, the magnitude of these two harmonics are larger under un-chorded winding, and thus, the xy inductance is expected to be larger for the un-chorded A6P machine [24].

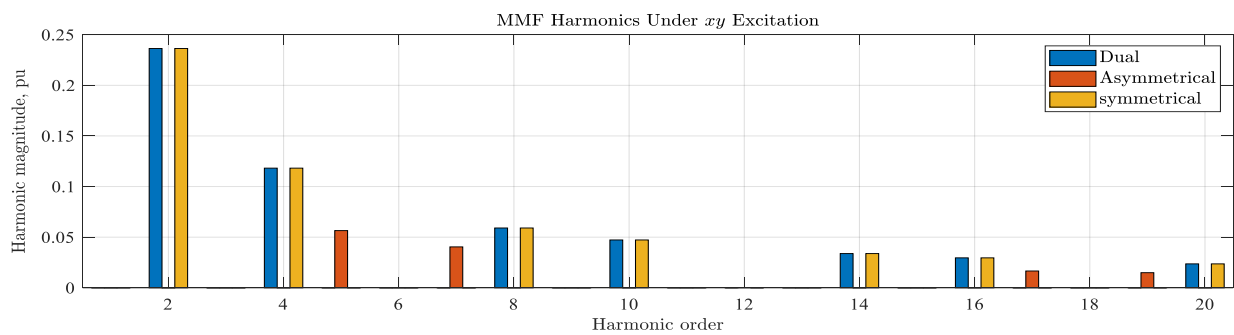


(a)

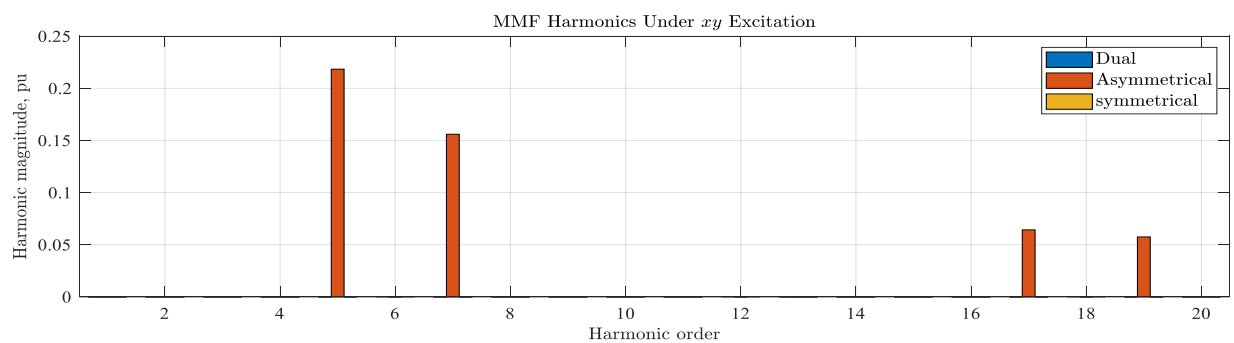


(b)

Figure 3. MMF harmonic spectra for different SPIM connections under $\alpha\beta$ excitation. (a) Chorded winding. (b) Un-chorded winding.



(a)



(b)

Figure 4. MMF harmonic spectra for different SPIM connections under xy excitation. (a) Chorded winding. (b) Un-chorded winding.

In the available literature [19], harmonic current compensation was proposed to suppress the induced harmonic current due to grid distortion. However, to the best of the authors' knowledge, literature has discarded the effect of the stator phase-belt harmonics on the current quality of the IOBC-based systems, which represents the main contribution of this study. It is expected that harmonic current compensation will be essential when even space harmonics are presenting in the stator airgap, which is the case for both D3P and S6P with chorded winding. Since no even harmonics are likely to present in the A6P stator, harmonics current compensation is not essential.

Under healthy operation, the $0^+ 0^-$ sequence components are controlled to zero, hence, their effect may be discarded. However, under postfault operation with one phase open, i_{0+0^-} components are used to ensure balanced, three-phase line currents, as shown in the next section. Under this latter case, the produced space harmonics due to this subspace should be taken into consideration. Figure 5 shows the MMF spectra under $0^+, 0^-$ sequence excitation. Under this excitation profile, the spectra of the three winding layouts seem to be the same for both chorded/un-chorded machines.

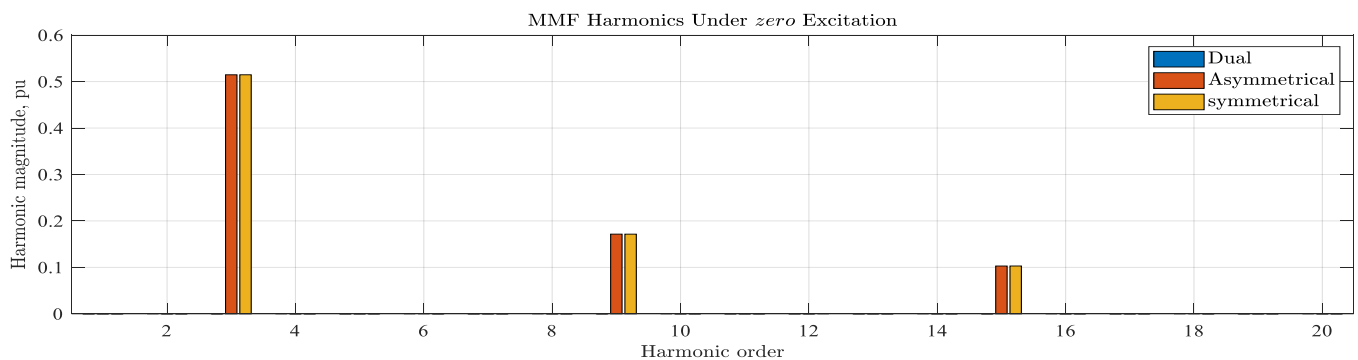


Figure 5. MMF harmonic spectra for different SPIM connections under zero – sequence excitation.

4. Optimal Current Derivation

The well-established VSD transformation [24] has been introduced to elaborate the relation between electrical and mechanical quantities and to introduce a simple method to design basic controllers. Using the VSD transformation given by (1), the physical phase quantities $f_s^{a_n \rightarrow c_n}$, where $f \in \{v, i\}$, v : voltage, and i : current, are decomposed into orthogonal stationary frames as given by (2). In this section, the optimal current derivation under both healthy and 1OPF under charging mode is introduced.

4.1. Optimal Currents Derivation under Healthy Mode

Referring to Section 2, and the phasor diagram given by Figure 1 under healthy case, the optimal phase currents can be obtained using (3), where each grid line current is constrained to its corresponding related pair of phase currents, as clear from Figure 2.

$$\begin{bmatrix} i_g^a \\ i_g^b \\ i_g^c \end{bmatrix} = \begin{bmatrix} 1 & 0 & 0 & 0 & 1 & 0 \\ 0 & 1 & 0 & 0 & 0 & 1 \\ 0 & 0 & 1 & 1 & 0 & 0 \end{bmatrix} \begin{bmatrix} i_s^{a1} \\ i_s^{b1} \\ i_s^{c1} \\ i_s^{a2} \\ i_s^{b2} \\ i_s^{c2} \end{bmatrix} \quad (3)$$

Under xy excitation, the phase current vector is given by (4).

$$\begin{bmatrix} i_s^{a1} \\ i_s^{b1} \\ i_s^{c1} \\ i_s^{a2} \\ i_s^{b2} \\ i_s^{c2} \end{bmatrix} = T_{VSD}^{-1} \begin{bmatrix} i_s^{\alpha\beta} \\ i_s^{xy} \\ i_s^{0+0-} \end{bmatrix}_{6 \times 1} = T_{VSD}^{-1} \begin{bmatrix} 0 \\ 0 \\ I \angle 0^\circ \\ I \angle 90^\circ \\ 0 \\ 0 \end{bmatrix} \quad (4)$$

From Figure 2, the grid current i_s^a is the summation of phase currents i_s^{a1} and i_s^{b1} . Hence, the relation between the resultant grid line current magnitude and machine phase current can be written as in (5).

$$|i_s^a| = 2|i_s^{a1}| \cos(\varphi/2) \quad (5)$$

where φ is the phase angle between each pair of phase currents, which equals 60° , 30° , and 0° for D3P, A6P, and S6P configurations, respectively.

From (3) and (4), the following conclusions could be made:

- The charging current flows through the machine at zero torque production, which, in turn, eliminates the need for interlocking mechanisms during the charging process. Besides, the xy subspace currents can be considered as the exclusive charging current components, which, when controlled according to (3), balanced grid currents are obtained, assuming that there is no asymmetry in the machine windings. According to the battery specifications, the reference current is predefined, and hence, the charging grid currents are determined.
- For a six-phase system, there is a total of five degrees of freedom. There are four reserved degrees of freedom (DOF) under charging mode ($i_s^{\alpha\beta}$ and i_s^{xy}) to nullify the average torque, while maintaining balanced grid currents. Hence, an extra degree of freedom ($i_0^+ = -i_0^-$) is still available, which can be used to maintain the same control objectives under 1OPF condition.

4.2. Postfault Optimal Current Derivation under 1OPF

Under 1OPF, one degree of freedom will be lost. The single remaining degree of freedom under healthy case can, therefore, be used to ensure the same control objectives.

Assuming phase- a_1 is the faulty phase ($i_s^{a1} = 0$), from the inverse of (2), one can write:

$$i_s^{a1} = i_s^\alpha + i_s^x + i_s^{0+} = 0 \quad (6)$$

Hence, the only condition that ensures same sequence current constraints of the healthy case is to have

$$i_s^{0-} = -i_s^{0+} = -i_s^x \quad (7)$$

The corresponding optimal currents under 1OPF can be obtained based on (8).

$$\begin{bmatrix} i_s^{a1} \\ i_s^{b1} \\ i_s^{c1} \\ i_s^{a2} \\ i_s^{b2} \\ i_s^{c2} \end{bmatrix} = T_{VSD}^{-1} \begin{bmatrix} i_s^{\alpha\beta} \\ i_s^{xy} \\ i_s^{0+0-} \end{bmatrix}_{6 \times 1} = T_{VSD}^{-1} \begin{bmatrix} 0 \\ 0 \\ I \angle 0^\circ \\ I \angle 90^\circ \\ I \angle 180^\circ \\ 0 \end{bmatrix} \quad (8)$$

Hence, the optimal currents for the three cases, assuming same pre-fault conditions, are given in Table 1. Under fault conditions, some phases will exceed their rated value in case a same rated charging current is required. Hence, a suitable derating should be applied based on the phase current having maximum phase magnitude (written in bold in

Table 1). The percentage derating to limit the phase having maximum current to 1 pu is also given in the same table.

Table 1. Optimal currents and derating percentages of different SPIM connections under 1OPF.

Connection	D3P	A6P	S6P
Optimal currents	$\begin{bmatrix} 0 \\ 1.7321\angle 150^\circ \\ 1.7321\angle -150^\circ \\ 0 \\ 1.7321\angle -30^\circ \\ 1.7321\angle 30^\circ \end{bmatrix}$	$\begin{bmatrix} 0 \\ 1.7321\angle 150^\circ \\ 1.7321\angle -150^\circ \\ 0.5176\angle -75^\circ \\ 1.9319\angle -15^\circ \\ 1.4142\angle 45^\circ \end{bmatrix}$	$\begin{bmatrix} 0 \\ 1.7321\angle 150^\circ \\ 1.7321\angle -150^\circ \\ 1\angle -60^\circ \\ 2\angle 0^\circ \\ 1\angle 60^\circ \end{bmatrix}$
Percentage derating (%)	42.3	48.2	50

5. Proposed General Current Proportional Resonant-Based Controller

In most available literature, conventional PR or synchronous PI controllers are shown to be suitable in grid connection and drive applications [25,26]. The same current controller structure can be preserved under both propulsion and charging modes through exciting the proper subspace according to the desired mode of operation. Hence, a PR current controller will be employed in this study.

Figure 6 shows the block diagram of the proposed PR-based general current controller. Although the control algorithm is the same for all the three configurations, the harmonic compensating (HC) voltage terms depend on the machine winding layout. The proposed controller consists of three main stages. In the first stage, the reference sequence current components are derived based on the reference dq grid current components, where the reference i_d^* component controls the charging level, while i_q^* is set to zero to ensure unity power factor. The corresponding reference $\alpha\beta$ grid currents, $i_g^{\alpha\beta*}$, are then obtained using the inverse Park’s transformation, while synchronization with the grid is simply done using a phase-locked loop. The stator xy reference currents are set equal to the $\alpha\beta$ grid currents, $i_g^{\alpha\beta*}$. It is noteworthy from Figure 1 that any grid line current is leading the corresponding phase current of the first three-phase set by an angle $\varphi/2$. Therefore, in order to achieve a unity power factor charging, $i_g^{\alpha\beta*}$ should be aligned with the grid voltage by rotating the machine reference i_{xy}^* current components by the same angle, $\varphi/2$. The fundamental subspace sequence currents, $i_{\alpha\beta}$, of the SPIM are set to zero to ensure zero torque production. Finally, i_{0+0-} components are set to zero under healthy conditions, whereas the reference values of this subspace are derived based on (7) under 1OPF.

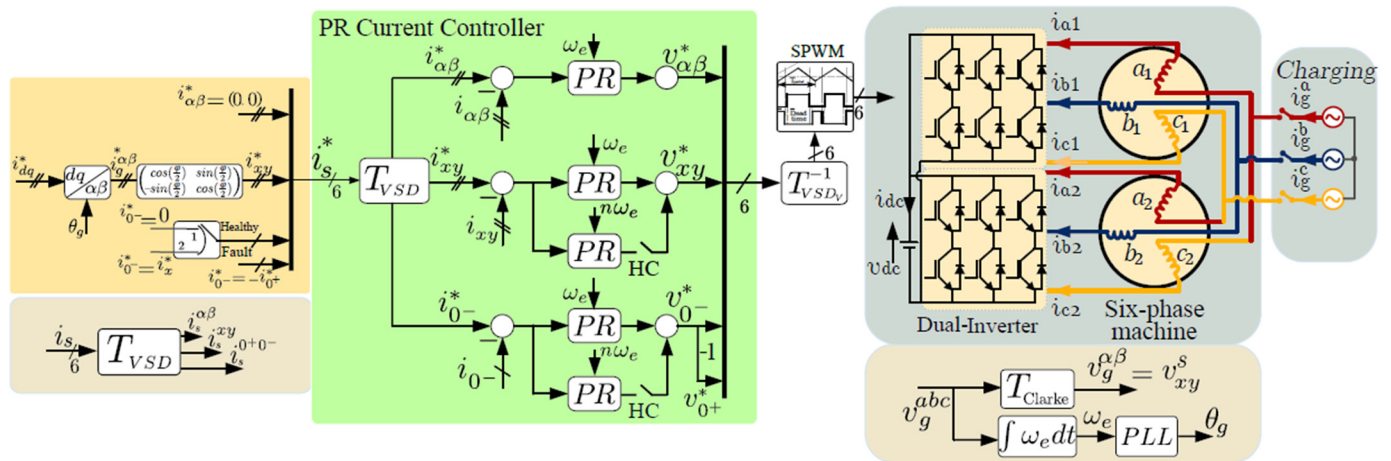


Figure 6. Proposed current controller of the six-phase-based non-isolated IOBC.

The second stage represents the PR-based current controllers, where a pair of PR controllers are used to control each subspace. Since $i_{0^+} = -i_{0^-}$, a single PR controller is used to derive the $0^+ 0^-$ sequence voltage components ($v_{0^+} = -v_{0^-}$). In both the xy and $0^+ 0^-$ subspaces, additional pairs of PR controllers are also used to compensate for the dominant low order harmonic current component induced in these subspaces. The harmonic compensation is enabled via HC switches shown in Figure 6. According to experimentation, the 5th and 3rd harmonics are the dominant harmonics in the xy and $0^+ 0^-$ subspaces, respectively.

In the third controller stage, the output voltage components of the PR controllers are transformed to their phase quantities using the inverse transformation given by (1). Conventional SPWM is then used to derive the six-phase inverter.

Under postfault operation, the same controller structure is used, which represents the main advantage of the proposed PR current controller. Referring to the analysis given in Section 4, only the reference value of the $0^+ 0^-$ subspace is changed to be $-i_x^*$ instead of zero under healthy case.

6. Experimental Evaluation

6.1. Experimental Setup

The proposed SPIM-based IOBC with different winding layouts has experimentally been validated using the test-rig shown in Figure 7. Two identical 24-slot, 4-pole off-the-shelf three-phase IMs have been rewound into chorded and un-chorded twelve-phase machines with the same rated current, as proposed in [24]. These two twelve-phase machines have been designed to be externally configured as a six-phase machine with the three possible winding configurations, namely D3P, A6P, or S6P. The first machine is wound as a double layer winding with a 5/6 coil span, while fully pitched coils are used with the second machine. The ratings of both machines are given in Table 2. Meanwhile, the measured machine parameters of both machines, which have been estimated using the technique introduced in [24], are given in Table 3. The power converter is built using a two-level six-phase inverter fed from a 300V programmable DC supply. Conventional SPWM at 5 kHz is used to derive the power converter. The controller was developed using the MATLAB/Simulink platform and deployed using Embedded Coder of Simulink into Texas Instruments F28379D Launchpad. The current feedback was carried out using six LEM LTS-25np hall effect sensors.

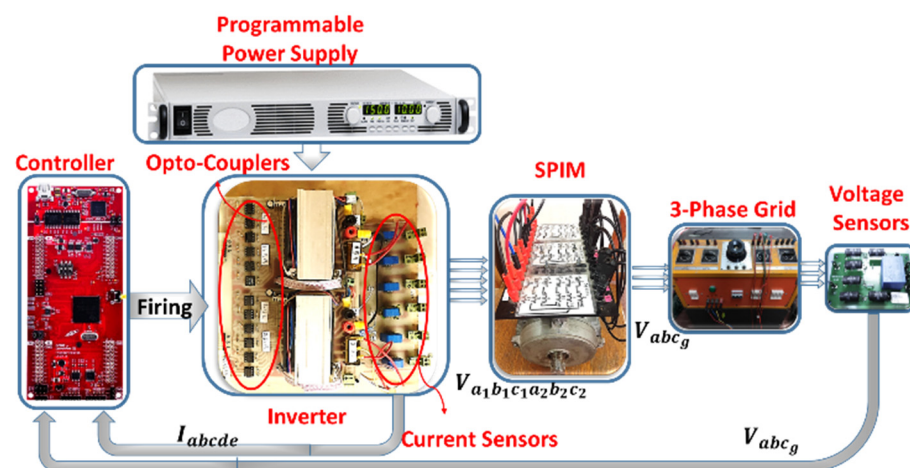


Figure 7. Experimental six-phase setup.

Table 2. Machine Ratings.

Parameter	Value
Rated RMS phase Voltage (V)	110 V
Rated Power (kW)	1.1
Rated RMS phase current (A)	2.8
Rated frequency (Hz)	50
No. of poles	4
Rated speed (RPM)	1400

Table 3. Machine Parameters.

Parameter	Chorded			Un-Chorded		
	D3P	A6P	S6P	D3P	A6P	S6P
Stator resistance	4.18 Ω	4.18 Ω	4.18 Ω	5 Ω	5 Ω	5 Ω
Rotor resistance	3.46 Ω	3.67 Ω	3.46 Ω	2.9 Ω	3.1 Ω	2.9 Ω
$\alpha\beta$ stator leakage inductance	9.1 mH	12 mH	9.1 mH	10 mH	9.6 mH	10 mH
$\alpha\beta$ rotor leakage inductance	19.1 mH	16.7 mH	19.1 mH	21 mH	22.5 mH	21 mH
$\alpha\beta$ magnetizing inductance	254 mH	247 mH	260 mH	270 mH	304 mH	284 mH
xy stator leakage inductance	11.8 mH	7.5 mH	11.8 mH	4.44 mH	25.5 mH	4.52 mH
Zero sequence resistance	5.5 Ω	13.7 Ω	5.6 Ω	5.6 Ω	6.7 Ω	6.86 Ω
Zero sequence inductance	18.2 mH	23.5 mH	26.2 mH	4.74 mH	26.46 mH	4.78 mH

6.2. Experimental Results

In this section, the experimental results of the SPIM-based IOBC are investigated under both healthy and fault conditions. In all cases, the same reference charging current is set according to (5) to the rated machine phase current (4A peak). The effect of harmonic compensation on the quality of the line currents is also assessed. In the following, all currents are given in per-unit values based on machine ratings given in Table 2.

6.2.1. Healthy Case

In this case, the effect of the $0^+ 0^-$ subspace can be discarded since its reference current components are $i_{0^+ 0^-}^* = 0$. The need for harmonic compensation is decided based on the obtained current waveforms along with the MMF spectra given in Figures 3–5.

Chorded Winding Layout

Under healthy case, the chorded winding of the SPIM-based IOBC has successfully achieved balanced three-phase grid currents with unity power factor for the three configurations, as shown in Figure 8. As previously mentioned in Section 2, the grid current magnitudes are $2 \cos 30^\circ$, $2 \cos 15^\circ$, and $2 \cos 0^\circ$ times the phase current magnitude under D3P, A6P, and S6P winding layout, respectively, as shown in Figure 9.

Clearly, both D3P and S6P machines correspond to a notable distortion in the current waveforms because of the even order space harmonics under xy excitation. Fourier analysis shows a dominant 5th harmonic component in the current spectra. On the other hand, the current quality of the A6P is much better. Therefore, a harmonic compensation technique has been applied to both D3P and S6P machines to enhance the current quality, as shown in Figure 10. The THD values and the magnitude of the 5th harmonic of both phase and line currents of each configuration with and without harmonic compensation are tabulated in Table 4.

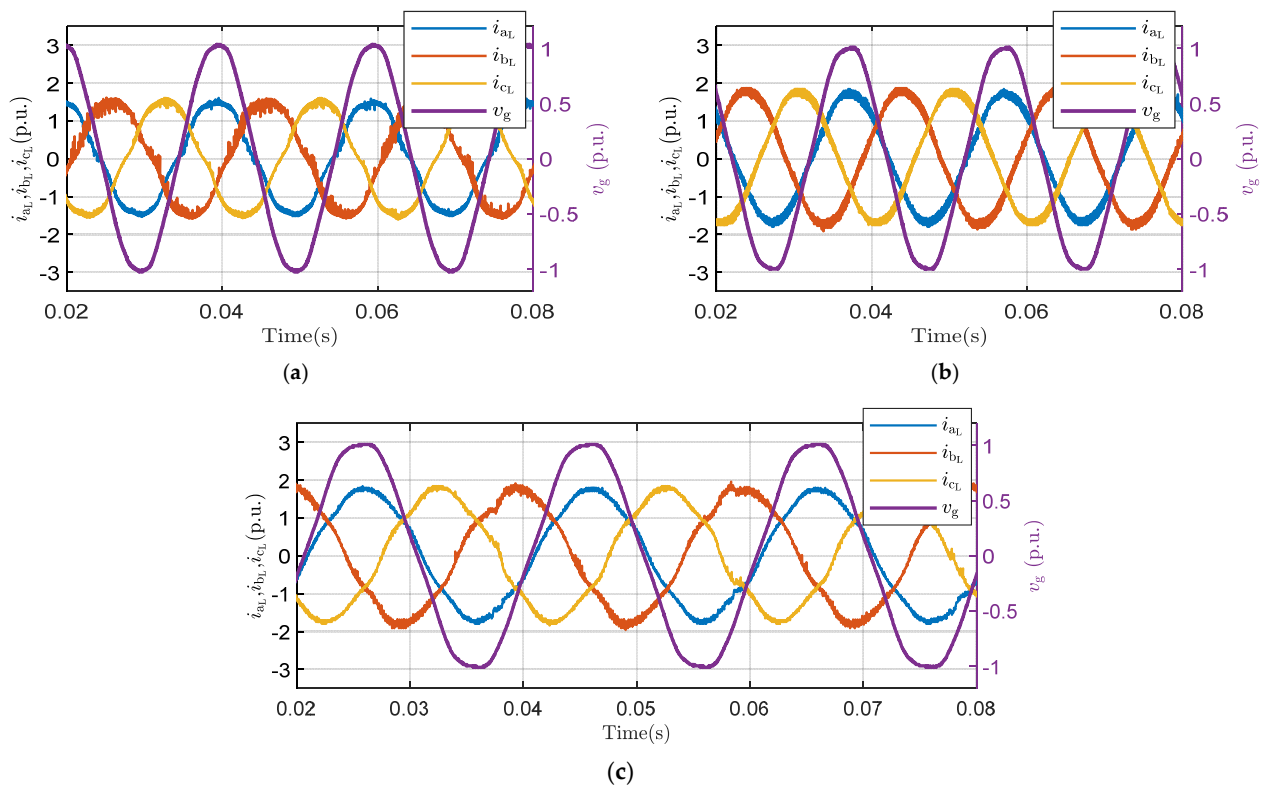


Figure 8. The grid line currents of chorded SPIM-based IOBC under healthy case without harmonic compensation. (a) D3P. (b) A6P. (c) S6P.

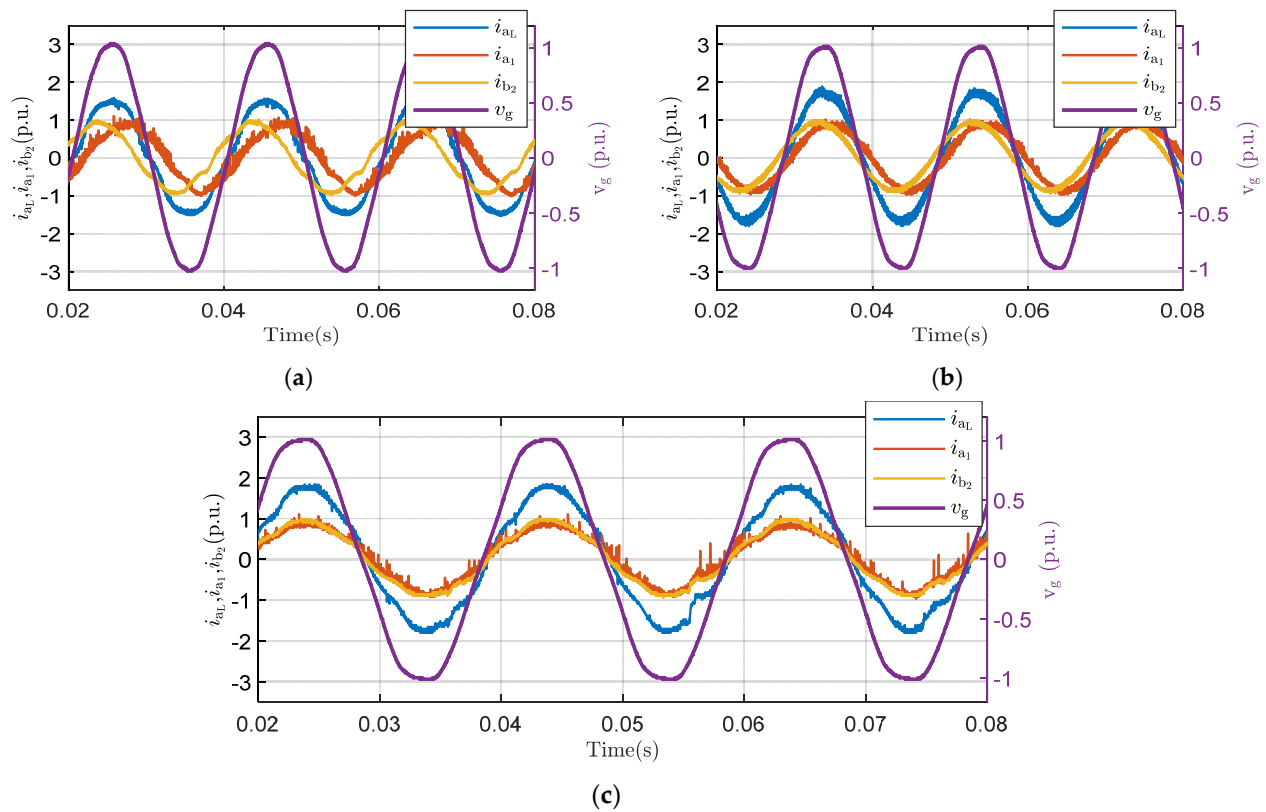


Figure 9. The phase to line current relation of chorded SPIM-based IOBC under healthy case without harmonic compensation. (a) D3P. (b) A6P. (c) S6P.

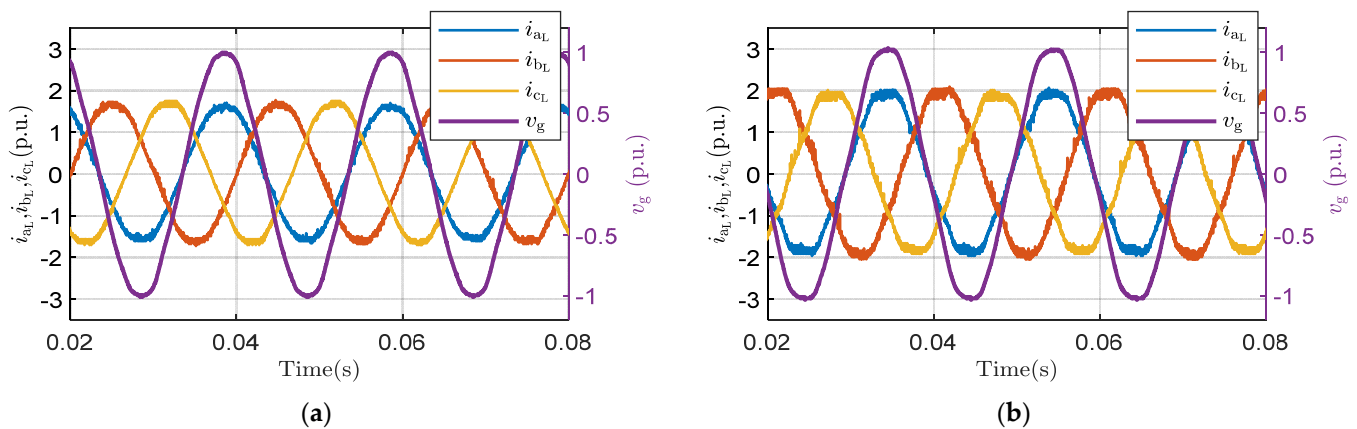


Figure 10. The grid line currents of chorded SPIM-based IOBC under healthy case with harmonic compensation. (a) D3P. (b) S6P.

Table 4. THD values of chorded SPIM-based IOBC under healthy operation.

THD	Without Harmonic Compensation			With Harmonic Compensation	
	D3P	A6P	S6P	D3P	S6P
THD Line current	5.01%	3.07%	5.05%	4.07%	3.93%
5th Har Mag.	3.89%	0.23%	3.71%	0.15%	0.25%
THD Phase current	6.24%	4.6%	5.6%	5%	5.17%
5th Har Mag.	3.87%	1.25%	3.48%	2%	0.38%

Un-Chorded Winding Layout

The same control technique has been applied to the un-chorded machine with its three possible configurations. The controller works efficiently and ensures balanced grid line currents with the same line-to-phase current magnitude ratios as in the chorded case, as shown in Figures 11 and 12. Unlike the chorded machine case with either D3P or S6P connections, Figure 11 shows that the current quality of the un-chorded machine is much better since the corresponding MMF spectra have no even harmonics. On the other hand, the ripple content in the current waveform is much higher because the corresponding inductance of the xy subspace will be much lower than the chorded machine, as is clear from the machine parameters given in Table 3. The THD values of the phase and line currents as well as the magnitude of the 5th harmonic given in Table 5 also ensure that the current quality of the un-chorded machines is better. Increasing the switching frequency can significantly decrease the magnitude of current ripples. On the other hand, the A6P phase and line currents have the best quality in the un-chorded machine since it corresponds to higher xy leakage inductance.

Table 5. THD values of un-chorded SPIM-based IOBC under healthy operation.

THD	Without Harmonic Compensation		
	D3P	A6P	S6P
THD Line current	7.69%	2.30%	7.26%
5th Har. Mag.	0.38%	0.26%	0.63%
THD Phase current	8.42%	3.25%	9.97%
5th Har. Mag.	0.29%	0.36%	0.36%

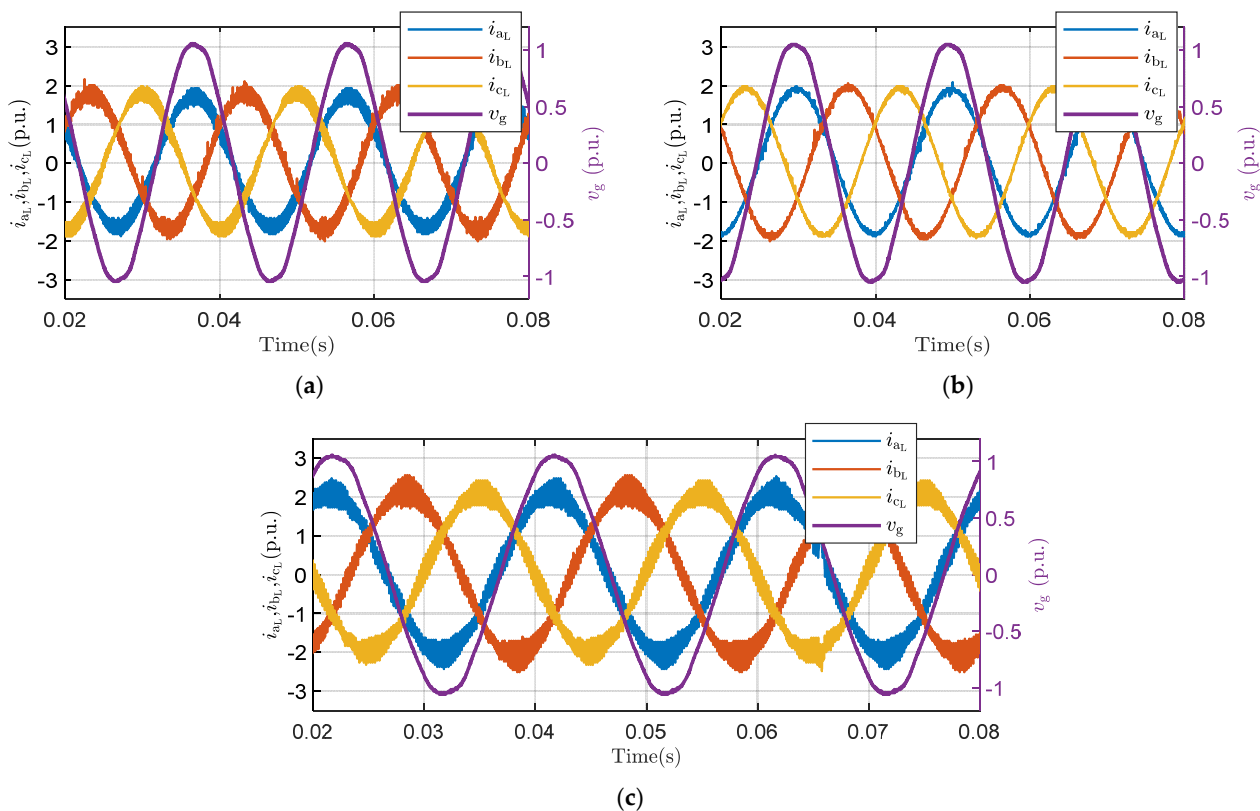


Figure 11. The grid line currents of un-chorded SPIM-based IOBC under healthy case. (a) D3P. (b) A6P. (c) S6P.

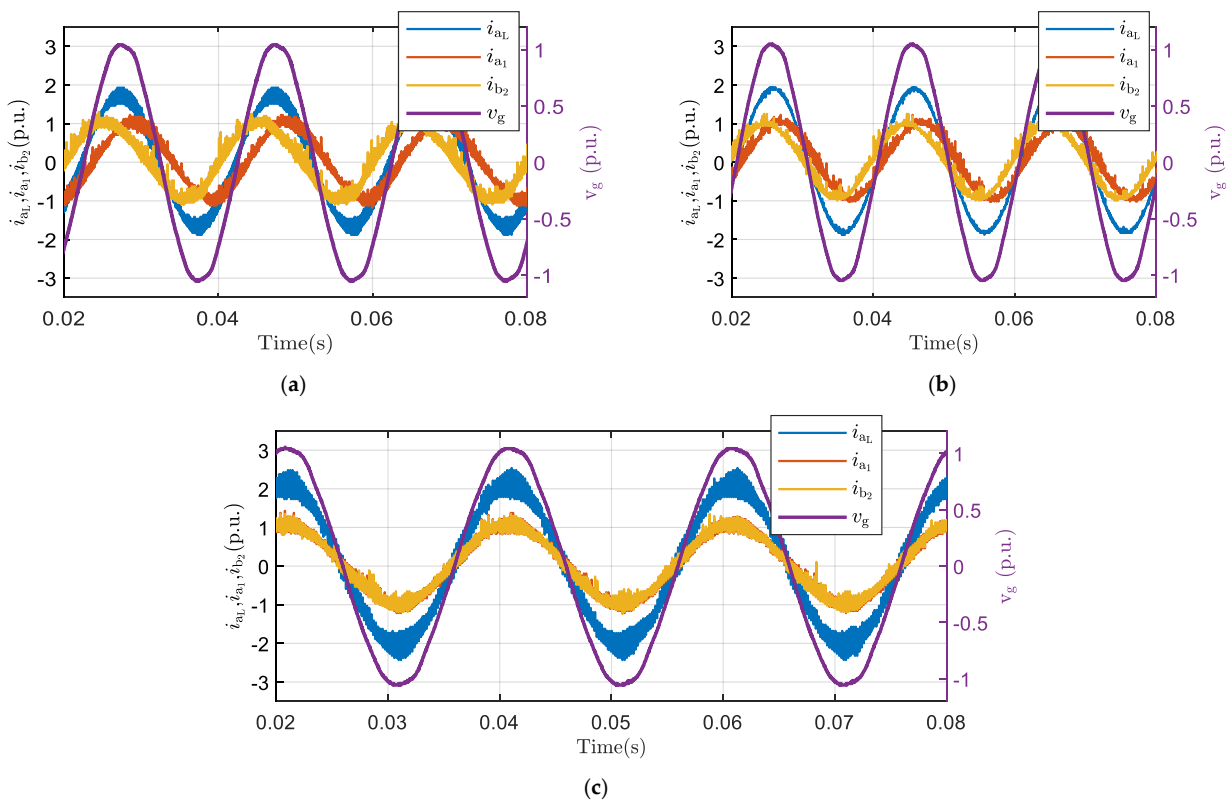


Figure 12. The phase and line current of un-chorded SPIM-based IOBC under healthy case. (a) D3P. (b) A6P. (c) S6P.

6.2.2. Post Fault Case

When a single open phase fault is detected and cleared, the postfault algorithm is initiated. The results shown in this subsection are given under postfault operation. The maximum allowable reference charging current will differ based on winding configuration to ensure that the stator currents shall not exceed the rated currents, which is 2.8 A(rms) = 1 p.u. The required percentage derating for each configuration is obtained based on Table 1.

Chorded Winding Layout

Figure 13 shows the grid line current of the three configurations under 1OPF. Figure 14 shows the uncompensated phase currents i_s^{a1} and i_s^{b2} with the corresponding grid line current i_g^a for the three configurations. From Figure 5, the $0^+ 0^-$ sequence component under 1OPF adds to phase current distortion due to the induced third harmonic current component. For this fault case, the third harmonic compensation is necessarily applied to the A6P and S6P to improve the current quality, while it is not needed for the D3P case, as shown in Figure 15. The THD values and the magnitude of the 5th and 3rd harmonics of the chorded machine under 1OPF of each configuration with/without harmonic compensation are shown in Table 6. It worth mentioning that the high THD of the A6P machine is due to the small leakage inductance of the xy subspace and, hence, the ripple current content is higher than D3P and S6P machines.

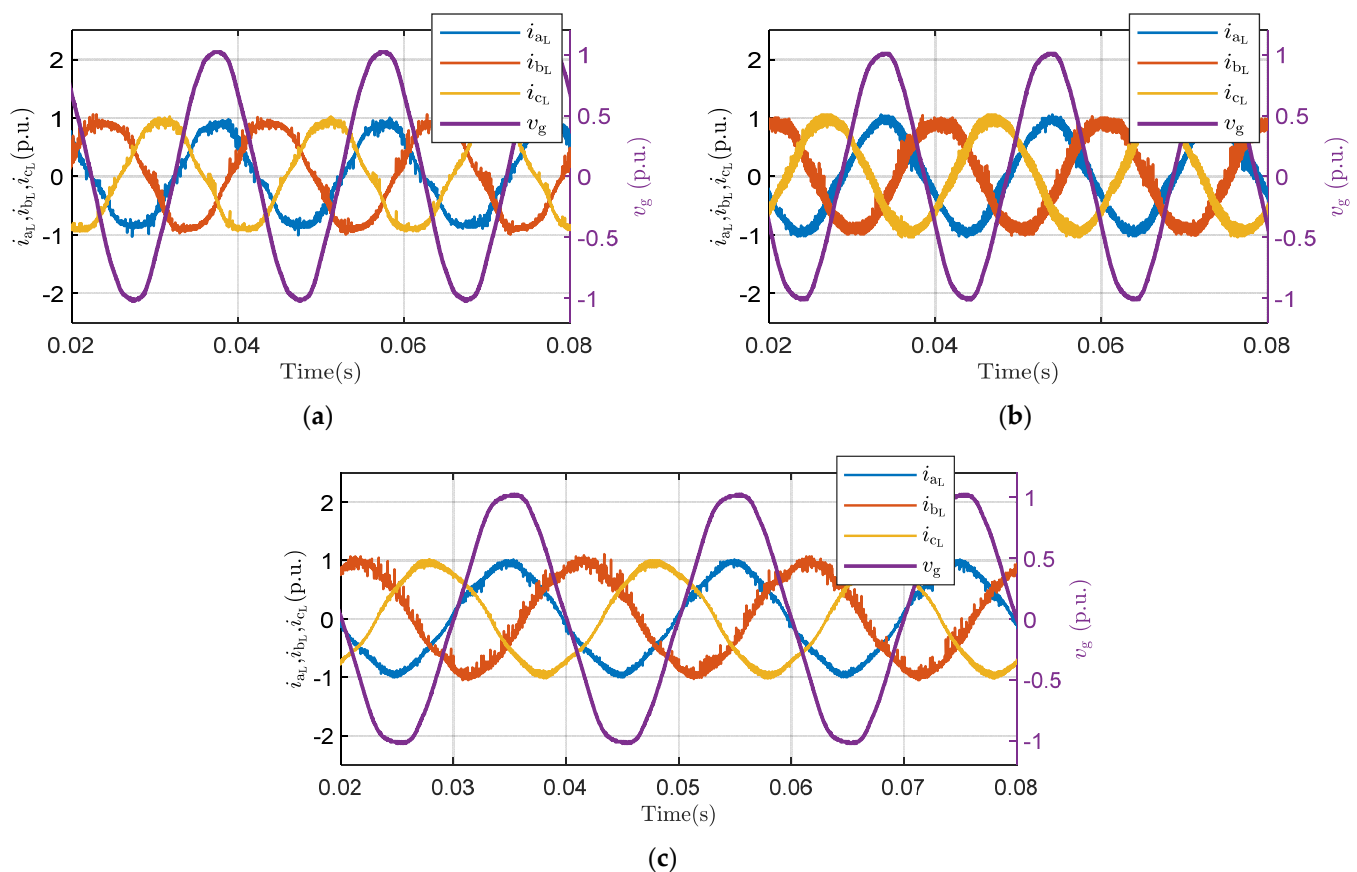


Figure 13. The grid line currents of chorded SPIM-based IOBC under 1OPF case without harmonic compensation. (a) D3P. (b) A6P. (c) S6P.

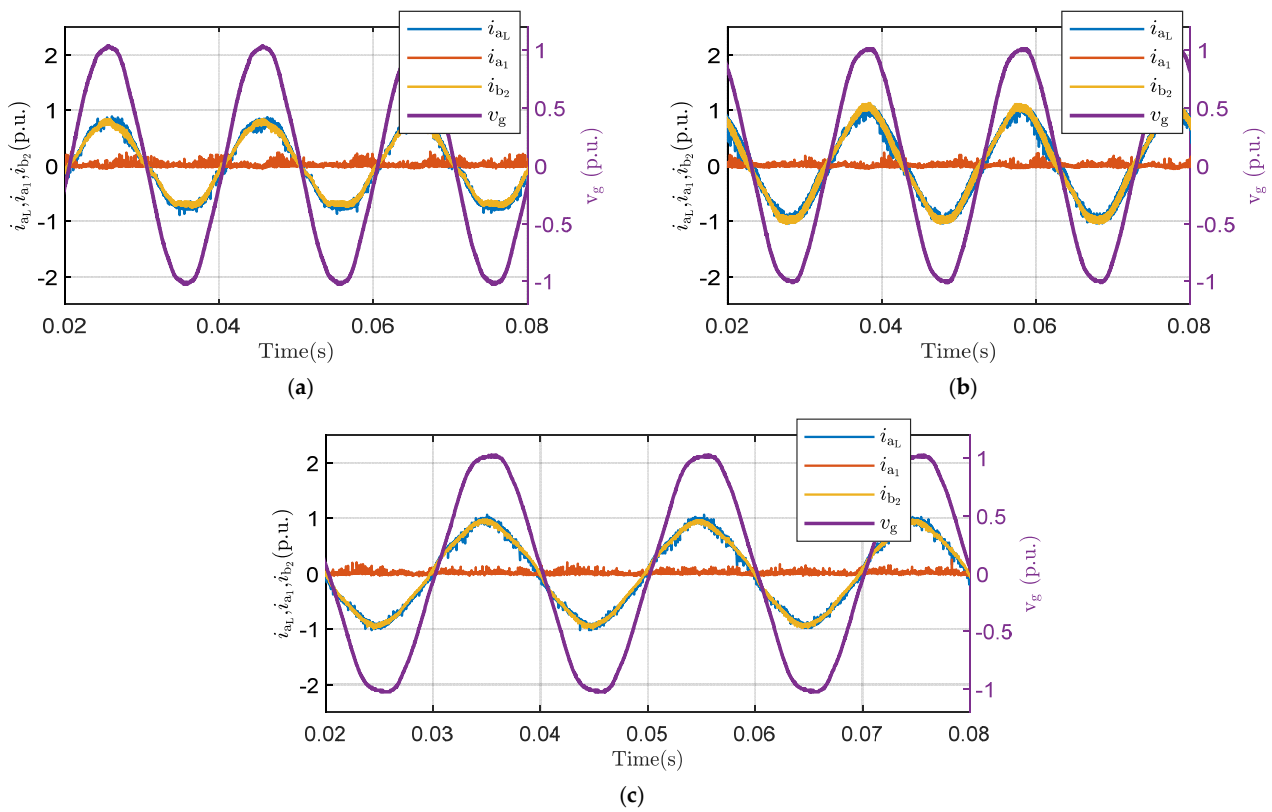


Figure 14. The phase and line currents of chorded SPIM-based IOBC under 1OPF case without harmonic compensation. (a) D3P. (b) A6P. (c) S6P.

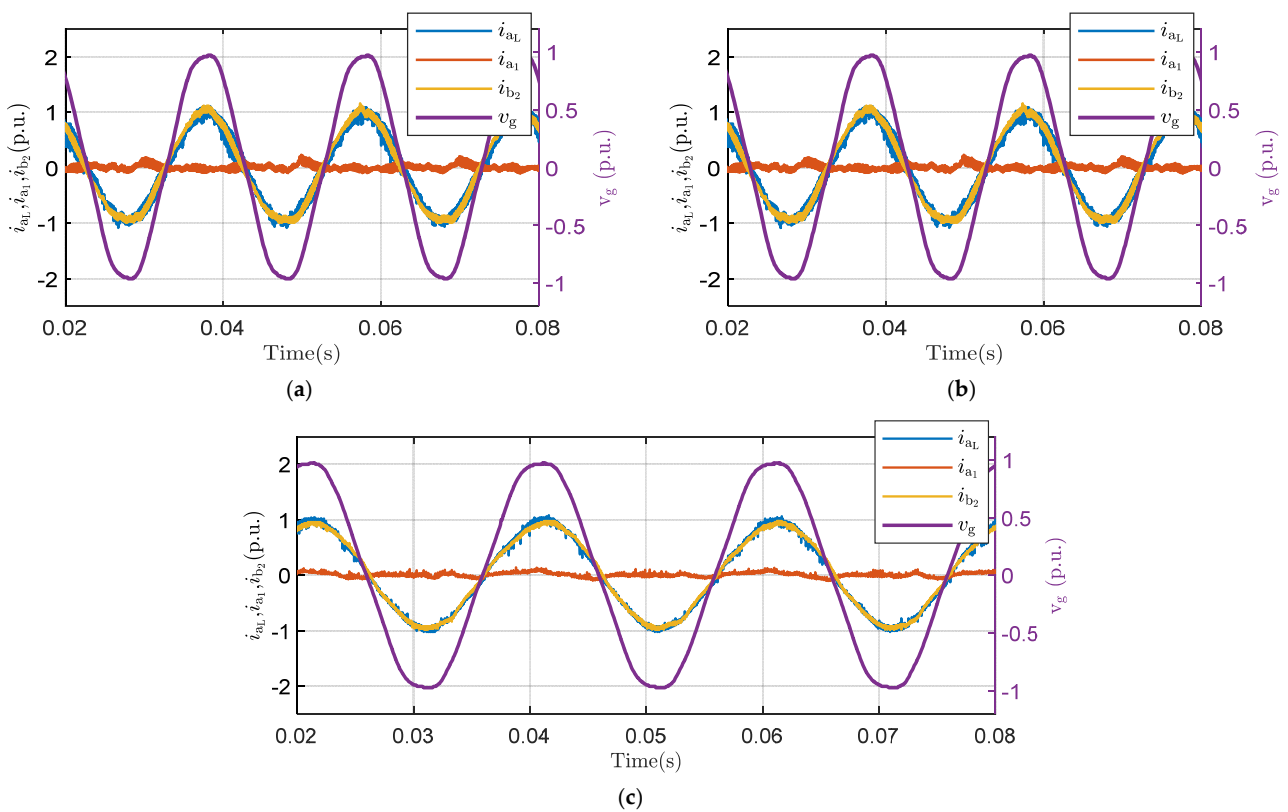


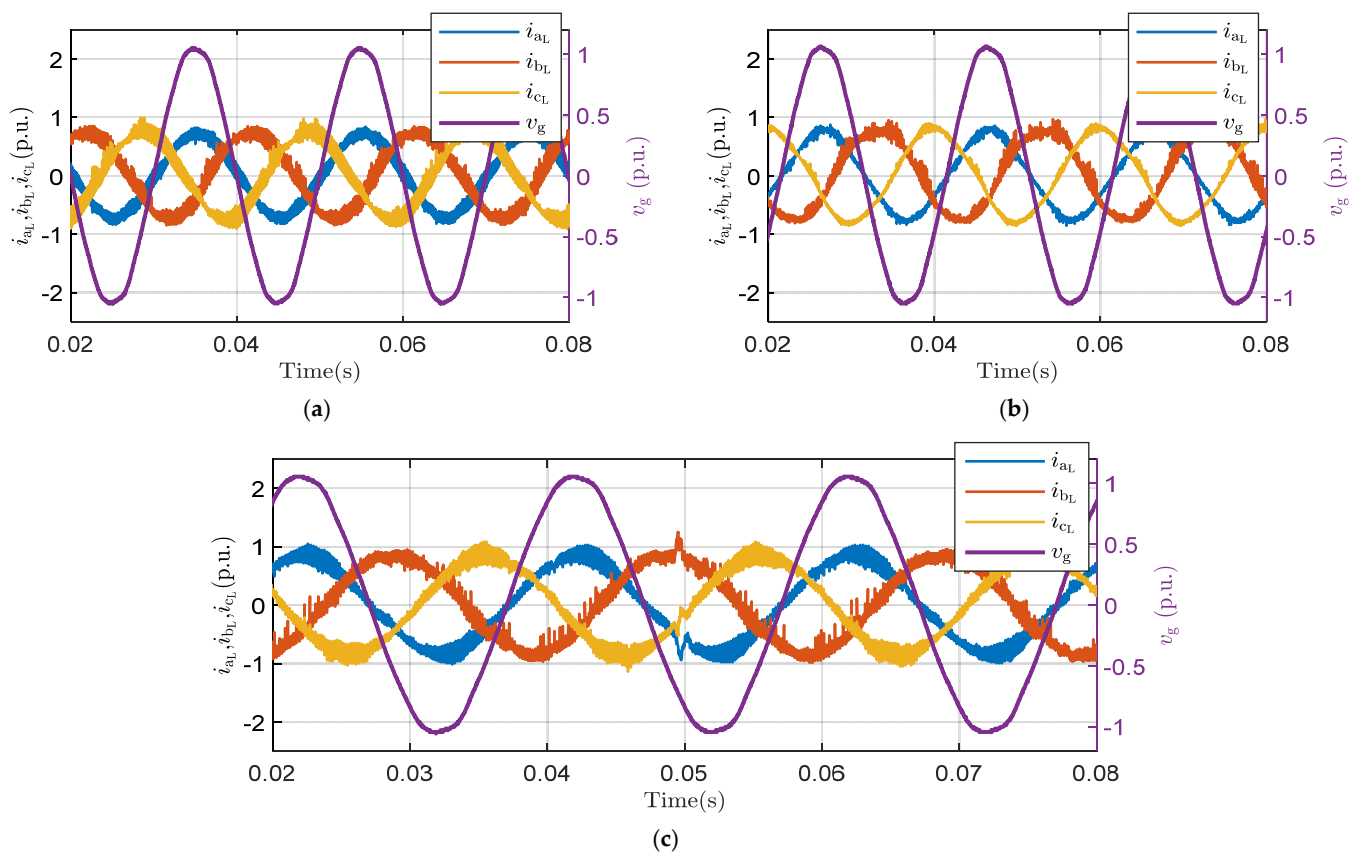
Figure 15. The phase and line currents of chorded SPIM-based IOBC under 1OPF case with harmonic compensation. (a) D3P. (b) A6P. (c) S6P.

Table 6. THD values of chorded SPIM-based IOBC under postfault operation (1OPF).

THD	Without Harmonic Compensation			With Harmonic Compensation		
	D3P	A6P	S6P	D3P	A6P	S6P
THD Line current	5.64%	10.67%	5.27%	5.95%	8.8%	5.14%
5th Har. Mag.	4.44%	0.21%	3.02%	0.82%	0.31%	0.14%
3rd Har Mag.	1.56%	2.84%	2.14%	1.56%	1.1%	1.56%
THD Phase current	6.13%	9.59%	8.33%	5.95%	8.98%	5.17%
5th Har Mag.	3.12%	1.33%	4.69%	0.82%	0.31%	0.38%
3rd Har Mag.	1.56%	3.39%	3.62%	1.56%	2.03%	0.3%

Un-Chorded Winding Layout

Similar to the chorded machine under 1OPF, the optimal currents are achieved through the excitation of both xy and $0^+ 0^-$ subspaces with optimal reference currents. Figure 16 shows the line charging currents of the un-chorded SPIM-based IOBC. The experimental results of the uncompensated case are similar to the chorded case, as shown in Figure 17. When third harmonic compensation is applied, the current waveforms are given in Figure 18, while the THD values for all cases are given in Table 7.

**Figure 16.** The grid line currents of un-chorded SPIM-based IOBC under 1OPF case. (a) D3P. (b) A6P. (c) S6P.

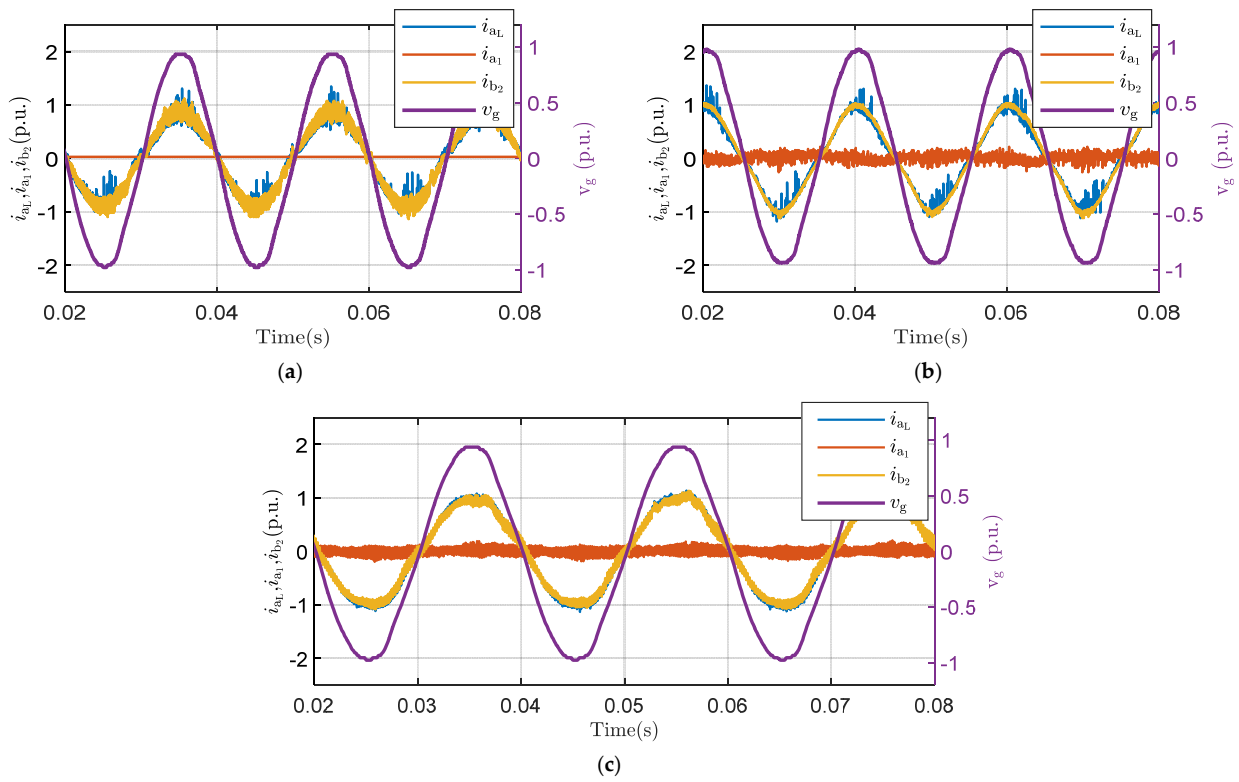


Figure 17. The phase and line currents of un-chorded SPIM-based IOBC under 1OPF case without harmonic compensation. (a) D3P. (b) A6P. (c) S6P.

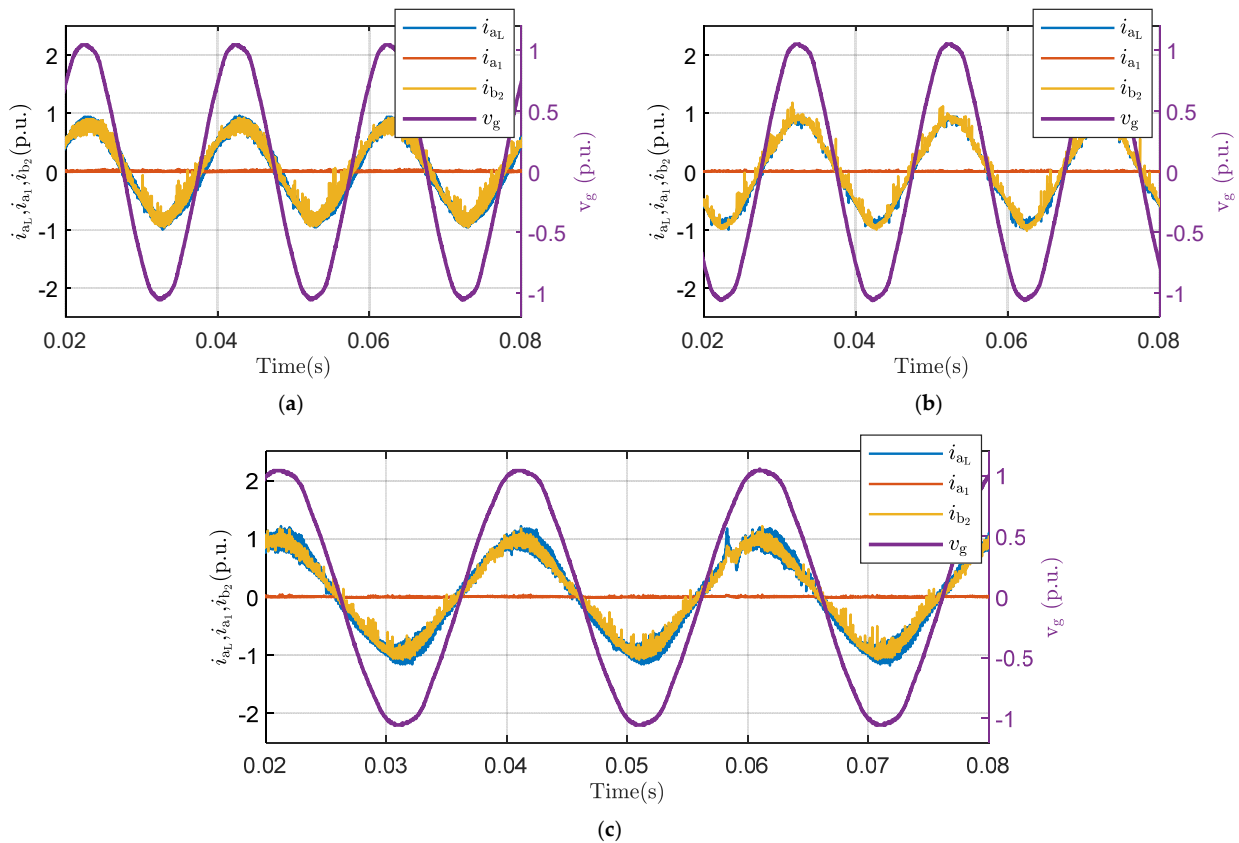


Figure 18. The phase and line currents of un-chorded SPIM-based IOBC under 1OPF case with harmonic compensation. (a) D3P. (b) A6P. (c) S6P.

Table 7. THD values of un-chorded SPIM based IOBC under postfault operation (1OPF).

THD	Without Harmonic Compensation			With Harmonic Compensation		
	D3P	A6P	S6P	D3P	A6P	S6P
THD Line current	11.13%	4.95%	11.86%	7.13%	2.91%	7.57%
5th Har Mag.	0.63%	0.95%	0.36%	0.63%	0.95%	0.36%
3rd Har Mag.	1.89%	0.7%	1.90%	1.89%	0.7%	1.90%
THD Phase current	7.64%	5.64%	10.01%	7.64%	3.23%	8.68%
5th Har Mag.	0.18%	1.64%	0.36%	0.18%	1.64%	0.36%
3rd Har Mag.	1.89%	6.5%	5.98%	1.89%	1.13%	1.20%

7. Conclusions

This paper investigated the effect of winding configuration on the performance of a SPIM-based non-isolated IOBC. The required stator connections to the grid were also suggested, which ensure minimum winding reconfigurations, maximum possible line to phase current magnitude ratio, and zero torque production. The maximum charging power percentages were therefore 86.6%, 96.5%, and 100% of the rated machine power for the D3P, A6P, and S6P configurations, respectively. The effect of the winding design (chorded or un-chorded designs) on the induced space harmonics was also clarified. Upon which, the required general current controller was derived that ensures high quality current waveforms. In the case of the chorded six-phase machine, the even low order space harmonics cause a notable current distortion and induce a notable 5th order harmonic current with the D3P and S6P cases. Whereas, although employing fully pitched coils cancels out all even order MMF space harmonics, the correspondent inductance of the xy subspace is significantly reduced, which increases the ripple content in the current waveform for the same switching frequency. The MMF spectrum of the A6P machine showed that in the case of either chorded or un-chorded six-phase machines, there is odd low order space harmonics which does not affect the machine current quality. The optimal phase currents and the required percentage derating under 1OPF has also been derived for the three possible connections. Under post-fault operation, 3rd harmonic compensation was needed in the A6P and S6P cases due to circulating i_{0+} i_{0-} components. A comparative case study has been carried out based on experiments to validate the theoretical findings. Furthermore, the low order harmonic current compensation has been introduced using additional pairs of PR controllers for each harmonic component (3rd and 5th). In conclusion, the results showed that the S6P configuration with un-chorded winding represents the best compromise in terms of line current magnitude and quality.

Author Contributions: Conceptualization: M.S.A.-M., A.S. and A.S.A.-K.; methodology: M.S.A.-M., A.S. and M.S.H.; software: M.S.A.-M., A.S. and M.M.S.; validation: M.S.A.-M., A.S. and N.A.E.; formal analysis: M.S.A.-M., A.S. and A.S.A.-K.; investigation: M.S.A.-M., A.S. and A.S.A.-K.; resources: M.S.H., M.M.S. and N.A.E.; data curation: M.S.A.-M., M.M.S. and N.A.E.; writing—original draft preparation: M.S.A.-M., A.S. and A.S.A.-K.; writing—review and editing: M.S.H., M.M.S. and N.A.E.; visualization: M.S.A.-M., A.S. and N.A.E.; supervision: M.S.H., M.M.S. and N.A.E.; project administration: A.S.A.-K. and M.S.H.; funding acquisition: A.S.A.-K. and M.S.H. All authors have read and agreed to the published version of the manuscript.

Funding: This research was funded by ITIDAs ITAC collaborative funded project under the category type of advanced research projects (ARP) and grant number ARP2020.R29.7.

Acknowledgments: This work was achieved through the financial support of ITIDAs ITAC collaborative funded project under the category type of advanced research projects (ARP) and grant number ARP2020.R29.7.

Conflicts of Interest: The authors declare no conflict of interest.

References

1. Williamson, S.S.; Rathore, A.K.; Musavi, F. Industrial electronics for electric transportation: Current state-of-the-art and future challenges. *IEEE Trans. Ind. Electron.* **2015**, *62*, 3021–3032. [\[CrossRef\]](#)
2. Liu, C.; Chau, K.; Wu, D.; Gao, S. Opportunities and challenges of vehicle-to-home, vehicle-to-vehicle, and vehicle-to-grid technologies. *Proc. IEEE* **2013**, *101*, 2409–2427. [\[CrossRef\]](#)
3. Metwly, M.Y.; Abdel-Majeed, M.S.; Abdel-Khalik, A.S.; Hamdy, R.A.; Hamad, M.S.; Ahmed, S. A review of integrated on-board EV battery chargers: Advanced topologies, recent developments and optimal selection of FSCW slot/pole combination. *IEEE Access* **2020**, *8*, 85216–85242. [\[CrossRef\]](#)
4. Na, T.; Yuan, X.; Tang, J.; Zhang, Q. A review of on-board integrated electric vehicles charger and a new single-phase integrated charger. *CPSS Trans. Power Electron. Appl.* **2019**, *4*, 288–298. [\[CrossRef\]](#)
5. Yilmaz, M.; Krein, P.T. Review of battery charger topologies, charging power levels, and infrastructure for plug-in electric and hybrid vehicles. *IEEE Trans. Power Electron.* **2012**, *28*, 2151–2169. [\[CrossRef\]](#)
6. Kim, D.-H.; Kim, M.-J.; Lee, B.-K. An integrated battery charger with high power density and efficiency for electric vehicles. *IEEE Trans. Power Electron.* **2016**, *32*, 4553–4565. [\[CrossRef\]](#)
7. Shi, C.; Tang, Y.; Khaligh, A. A three-phase integrated onboard charger for plug-in electric vehicles. *IEEE Trans. Power Electron.* **2017**, *33*, 4716–4725. [\[CrossRef\]](#)
8. Grunditz, E.A.; Thiringer, T. Performance Analysis of Current BEVs Based on a Comprehensive Review of Specifications. *IEEE Trans. Transp. Electrification* **2016**, *2*, 270–289. [\[CrossRef\]](#)
9. Abdel-Khalik, A.S.; Massoud, A.; Ahmed, S. Interior permanent magnet motor-based isolated on-board integrated battery charger for electric vehicles. *IET Electr. Power Appl.* **2018**, *12*, 124–134. [\[CrossRef\]](#)
10. Abdel-Majeed, M.S.; Eldeeb, H.M.; Metwly, M.Y.; Abdel-Khalik, A.S.; Hamad, M.; Hamdy, R.A.; Ahmed, S. Post-fault Operation of Onboard Integrated battery Charger via a Nine-Phase EV-Drive Train. *IEEE Trans. Ind. Electron.* **2020**, *7*, 5626–5637.
11. Melo, V.F.M.B.; Jacobina, C.B.; Rocha, N.; Braga-Filho, E.R. Fault tolerance performance of two hybrid six-phase drive systems under single-phase open-circuit fault operation. *IEEE Trans. Ind. Appl.* **2019**, *55*, 2973–2983. [\[CrossRef\]](#)
12. Subotic, I.; Bodo, N.; Levi, E. An EV Drive-Train With Integrated Fast Charging Capability. *IEEE Trans. Power Electron.* **2016**, *31*, 1461–1471. [\[CrossRef\]](#)
13. Subotic, I.; Levi, E. An integrated battery charger for EVs based on a symmetrical six-phase machine. In Proceedings of the 2014 IEEE 23rd International Symposium on Industrial Electronics (ISIE), Istanbul, Turkey, 1–4 June 2014; pp. 2074–2079.
14. Abdel-Khalik, A.S.; Massoud, A.; Ahmed, S. Standard Three-Phase Stator Frames for Multiphase Machines of Prime-Phase Order: Optimal Selection of Slot/Pole Combination. *IEEE Access* **2019**, *7*, 78239–78259. [\[CrossRef\]](#)
15. Paredes, J.; Prieto, B.; Satrustegui, M.; Elósegui, I.; González, P. Improving the Performance of a 1-MW Induction Machine by Optimally Shifting From a Three-Phase to a Six-Phase Machine Design by Rearranging the Coil Connections. *IEEE Trans. Ind. Electron.* **2021**, *68*, 1035–1045. [\[CrossRef\]](#)
16. Shawier, A.; Habib, A.; Mamdouh, M.; Abdel-Khalik, A.S.; Ahmed, K.H. Assessment of predictive current control of six-phase induction motor with different winding configurations. *IEEE Access* **2021**, *9*, 81125–81138. [\[CrossRef\]](#)
17. Abdel-Khalik, A.S.; Massoud, A.M.; Ahmed, S. An Improved Torque Density Pseudo Six-Phase Induction Machine Using a Quadruple Three-Phase Stator Winding. *IEEE Trans. Ind. Electron.* **2020**, *67*, 1855–1866. [\[CrossRef\]](#)
18. Subotic, I.; Levi, E.; Jones, M.; Graovac, D. An Integrated Battery Charger for EVs Based on an Asymmetrical Six-Phase Machine. In Proceedings of the IECON 2013-39th Annual Conference of the IEEE Industrial Electronics Society, Vienna, Austria, 10–13 November 2013; pp. 7244–7249.
19. Subotic, I.; Bodo, N.; Levi, E. Integration of six-phase EV drivetrains into battery charging process with direct grid connection. *IEEE Trans. Energy Convers.* **2017**, *32*, 1012–1022. [\[CrossRef\]](#)
20. Diab, M.S.; Elserougi, A.A.; Abdel-Khalik, A.S.; Massoud, A.M.; Ahmed, S. A nine-switch-converter-based integrated motor drive and battery charger system for EVs using symmetrical six-phase machines. *IEEE Trans. Ind. Electron.* **2016**, *63*, 5326–5335. [\[CrossRef\]](#)
21. Liu, X.; Yu, F.; Mao, J.; Yang, H. Pre-and post-fault operations of six-phase electric-drive-reconstructed onboard charger for electric vehicles. *IEEE Trans. Transp. Electrification* **2021**. [\[CrossRef\]](#)
22. Munim, W.N.W.A.; Duran, M.J.; Che, H.S.; Bermudez, M.; Gonzalez-Prieto, I.; Abd Rahim, N. A unified analysis of the fault tolerance capability in six-phase induction motor drives. *IEEE Trans. Power Electron.* **2016**, *32*, 7824–7836. [\[CrossRef\]](#)
23. Garcia, D.F.V.; Taylor, J.; Mohamadian, M.; Luedtke, D.; Emadi, A.; Bilgin, B. *A Comparative Analysis for Six-Phase Motor Configurations*; 0148-7191; SAE Technical Paper; SAE International: Warrendale, PA, USA, 2020.
24. Abdel-Khalik, A.S.; Abdel-Majeed, M.S.; Ahmed, S. Effect of winding configuration on six-phase induction machine parameters and performance. *IEEE Access* **2020**, *8*, 223009–223020. [\[CrossRef\]](#)
25. Vidal, A.; Freijedo, F.D.; Yepes, A.G.; Fernandez-Comesana, P.; Malvar, J.; López, Ó.; Doval-Gandoy, J. Assessment and optimization of the transient response of proportional-resonant current controllers for distributed power generation systems. *IEEE Trans. Ind. Electron.* **2012**, *60*, 1367–1383. [\[CrossRef\]](#)
26. Yepes, A.G.; Vidal, A.; Malvar, J.; López, O.; Doval-Gandoy, J. Tuning method aimed at optimized settling time and overshoot for synchronous proportional-integral current control in electric machines. *IEEE Trans. Power Electron.* **2013**, *29*, 3041–3054. [\[CrossRef\]](#)